

# Incommensurate magnetic orders and possible field-induced skyrmion state in the square-net centrosymmetric $\text{EuGa}_2\text{Al}_2$ system

Jaime M. Moya,<sup>1,2</sup> Shiming Lei,<sup>2,\*</sup> Eleanor M. Clements,<sup>3</sup> Caitlin S. Kengle,<sup>4</sup> Stella Sun,<sup>4</sup> Kevin Allen,<sup>2</sup> Qizhi Li,<sup>5</sup> Y.Y. Peng,<sup>5</sup> Ali A. Husain,<sup>6</sup> Matteo Mitrano,<sup>7</sup> Matthew J. Krogstad,<sup>8</sup> Raymond Osborn,<sup>8</sup> Anand B. Puthirath,<sup>9</sup> Songxue Chi,<sup>10</sup> P. Abbamonte,<sup>4</sup> Jeffrey W. Lynn,<sup>3</sup> and E. Morosan<sup>2,†</sup>

<sup>1</sup>*Applied Physics Graduate Program, Smalley-Curl Institute, Rice University, Houston, Texas 77005, USA*

<sup>2</sup>*Department of Physics and Astronomy, Rice University, Houston, TX, 77005 USA*

<sup>3</sup>*NIST Center for Neutron Research, National Institute of Standards and Technology, Gaithersburg, MD 20899, USA*

<sup>4</sup>*Department of Physics, University of Illinois at Urbana-Champaign, Urbana, IL USA*

<sup>5</sup>*International Center for Quantum Materials, School of Physics, Peking University, CN-100871, Beijing, China*

<sup>6</sup>*Department of Physics and Astronomy and Quantum Matter Institute,*

*University of British Columbia, Vancouver, British Columbia V6T 1Z1, Canada*

<sup>7</sup>*Department of Physics, Harvard University, Cambridge, Massachusetts 02138, USA*

<sup>8</sup>*Materials Science Division, Argonne National Laboratory, Lemont, IL, USA*

<sup>9</sup>*Department of Materials Science and NanoEngineering, Rice University, Houston, TX, 77005 USA*

<sup>10</sup>*Neutron Scattering Division, Oak Ridge National Laboratory, Oak Ridge, Tennessee 37831, USA*

(Dated: June 29, 2022)

Neutron diffraction on the centrosymmetric square-net magnet  $\text{EuGa}_2\text{Al}_2$  reveals multiple incommensurate magnetic states (AFM1,2,3) in zero field. In applied field, a new magnetic phase (A) is identified from magnetization and transport measurements, bounded by two of the  $H = 0$  incommensurate magnetic phases (AFM1, helical and AFM3, cycloidal) with different moment orientations. Moreover, magneto-transport measurements indicate the presence of topological Hall effect, with maximum values in the A phase. Together, these results render  $\text{EuGa}_2\text{Al}_2$  a material with non-coplanar or topological spin texture in applied field. X-ray diffraction reveals an out-of-plane (OOP) charge density wave (CDW) below  $T_{\text{CDW}} \sim 50$  K while the magnetic propagation vector lies in-plane below  $T_N = 19.5$  K. Together this data points to a new route to realizing in-plane non-collinear spin textures through an OOP CDW which may in turn be unstable against the formation of topological spin textures in an applied field.

Magnetic skyrmions are particle-like spin textures of topological origin, which exist in the real space of materials [1]. The intensive research activity on skyrmions has been driven not only by the interest in their fundamental physical properties, but also by their potential applications to next-generation memory, logic, and neuromorphic computing devices [2–4]. One prominent feature of magnetic skyrmions is that the current density required for the manipulation of their functionality is about five to six orders of magnitude less than in modern spintronics [1, 5], establishing them as promising candidates for the design of energy-efficient electronic devices.

Following the experimental discovery of magnetic skyrmions in non-centrosymmetric crystals [6–9], the existence of skyrmion lattices in centrosymmetric materials was quickly proposed theoretically and experimentally confirmed recently. Compared to the non-centrosymmetric materials, where the Dzyaloshinskii-Moriya (DM) interaction [10, 11] is widely accepted as a critical driving force in stabilizing skyrmions, the mechanism for the formation of skyrmions in centrosymmetric materials is less well understood. Theoretically, geometrically frustrated systems with short-range two-spin interactions were considered model candidates to host magnetic skyrmions [12–14]. Alternatively, the four-spin interaction mediated by itinerant electrons has also been emphasized as an important ingredient [15–18].

Despite substantive progress in the theoretical understanding of skyrmion formation in centrosymmetric materials, the actual mechanism in real materials is still under debate. The limiting factor is the small number of known centrosymmetric skyrmion materials. So far, these materials have been limited to several intermetallic Gd-based compounds, including  $\text{Gd}_2\text{PdSi}_3$  [19, 20] (triangular lattice),  $\text{Gd}_3\text{Ru}_4\text{Al}_{12}$  [21] (breathing Kagomé lattice), and  $\text{GdRu}_2\text{Si}_2$  [22, 23] (square lattice), as well as the perovskite oxide  $\text{SrFeO}_3$  (cubic lattice) [24, 25]. Particularly, the experimental discovery of  $\text{GdRu}_2\text{Si}_2$  and  $\text{SrFeO}_3$  as skyrmion hosts indicates that *geometric* frustration may not be a necessary ingredient for the stabilization of skyrmions in centrosymmetric materials. Following the discovery of skyrmions in  $\text{GdRu}_2\text{Si}_2$ , Nomoto *et al.* [26] studied the the formation mechanism of the helical spin structure in  $\text{GdRu}_2\text{Si}_2$  and  $\text{Gd}_2\text{PdSi}_3$  by first principle calculations, and concluded that the *interorbital* frustration inherent to Gd ions is the origin of the incommensurate spin modulation. By comparison, Hayami and Motome’s work [27] based on an effective spin model suggested that the interplay of the four-spin interaction, bond-dependent anisotropic interaction and easy-axis anisotropy was essential for skyrmion formation in a square lattice. Independently, Wang *et al.* [28] pointed out that multiple topological spin textures, including meron, skyrmion, and vortex crystals, can be

stabilized when only four-spin interactions and compass anisotropy are considered, without the need of a bare single-ion anisotropy. It is thus paramount that new skyrmion-hosting materials, particularly non-Gd-based compounds, are discovered and synthesized, in order to clarify the underlying mechanisms.

In this Letter, we report the observation of a nonzero topological Hall effect (THE) in the centrosymmetric square-lattice compound  $\text{EuGa}_2\text{Al}_2$ . The THE persists over a large range of magnetic field–temperature ( $H$ - $T$ ) space, peaking in an intermediate-field A phase. Neutron scattering measurements in zero field identify two magnetic phases (AFM1, AFM3), both with non-collinear spin configurations and incommensurate propagation wavevectors, with a third intermediate phase with a mixed wavevector (AFM2) separating AFM1 and AFM3. When a magnetic field is applied, the transition between AFM1 (with a helical spin configuration and an incommensurate propagation wavevector along the crystallographic  $a$  axis) and AFM3 (with a cycloidal spin texture and an incommensurate propagation vector along  $a$ ) occurs *via* the newly-discovered A phase, which is anticipated to have a non-coplanar spin texture or a skyrmion state, and is responsible for the observed THE. Furthermore, X-ray diffraction (XRD) measurements on  $\text{EuGa}_2\text{Al}_2$  reveal an out-of-plane (OOP) charge density wave (CDW) above  $T_N$  (preformed CDW) which persists even below  $T_N$ . Our combined magneto-transport and structural characterization in  $\text{EuGa}_2\text{Al}_2$  points to the important role of the preformed CDW in the formation of non-collinear spin textures, and suggests a possible new mechanism for the design of topological spin textures and nonzero THE in centrosymmetric materials.

$\text{EuGa}_2\text{Al}_2$  is an isostructural analog to the established skyrmion host  $\text{GdRu}_2\text{Si}_2$  [22, 23, 29] (Fig. 1a,b). Furthermore, the magnetism in the former originates in localised  $\text{Eu}^{2+}$  ions ( $4f^7$ ,  $J = 7/2$ ,  $L = 0$ ) [30], equivalent to  $\text{Gd}^{3+}$  [22]. The similarities between these two compounds extend to the complex magnetic order:  $\text{EuGa}_2\text{Al}_2$  shows multiple magnetic transitions in the zero field limit at  $T_N \approx 19.5$  K,  $T_2 \approx 15$  K, and  $T_3 \approx 11$  K [30]. The lack of single ion anisotropy and the existence of multiple magnetic phases in zero field point to several potentially-competing energy scales, which are required for skyrmion hosting materials. This observation, and the structural and magnetic similarities with  $\text{GdRu}_2\text{Si}_2$  in a non-Gd compound motivated us to further determine the  $H$ - $T$  phase diagram in  $\text{EuGa}_2\text{Al}_2$ .

When an external magnetic field is applied along  $H \parallel c$  (the direction of the OOP CDW modulation, as discussed below), the isothermal magnetization measurements  $M(H)$  reveal multiple field-induced transitions. Fig. 1c illustrates a  $M(H)$  curve measured at  $T = 2$  K (full symbols, left axis), where a new phase, not previously resolved (denoted as the A phase) is revealed in  $dM/dH$  for  $1.2 \text{ T} < \mu_0 H < 1.6 \text{ T}$  (open symbols,

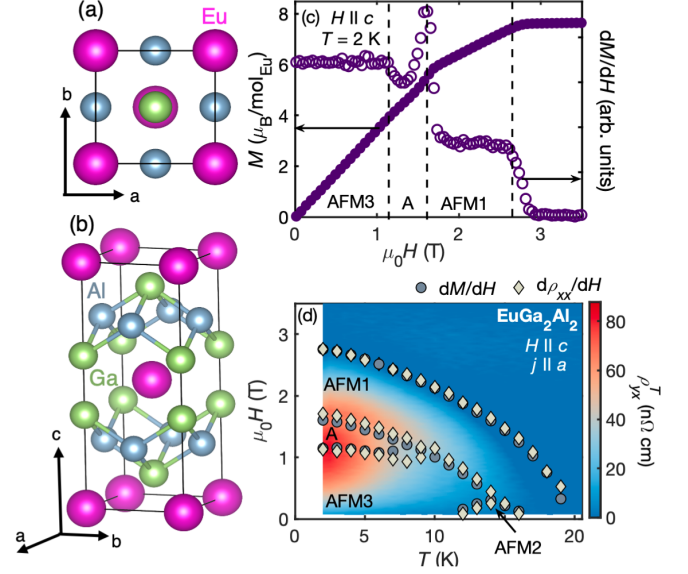


FIG. 1: Structure of  $\text{EuGa}_2\text{Al}_2$  and low temperature magnetic transitions. (a) and (b) top view and side view of  $\text{EuGa}_2\text{Al}_2$  structure. (c) Magnetic field dependent magnetization  $M$  measured at  $T = 2$  K with magnetic field  $H \parallel c$  (left axis, closed circles) and the corresponding differential magnetic susceptibility  $dM/dH$  (right axis, open circles). (d) The magnetic phase diagram constructed by local maxima in  $dM/dH$  (circles) and  $d\rho_{xx}/dH$  (diamonds) together with the contour map of  $\rho_{yx}^T$  established from Fig. 3. See text for details.

right axis). The  $H$ - $T$  phase diagram of  $\text{EuGa}_2\text{Al}_2$  for  $2 \text{ K} < T < 21.5 \text{ K}$  and  $0 \text{ T} < \mu_0 H < 3.5 \text{ T}$  derived from field-dependent magnetization  $M(H)$  (circles) and resistivity  $\rho_{xx}(H)$  (diamonds) is shown in Fig. 1d. The detailed determination of the transition parameters are presented in the Supplementary Materials. The three magnetic phases AFM1, AFM2, and AFM3 are consistent with previously published zero-field data [30], and the newly identified A phase is shown to exist in a narrow field range between 1.25 T and 1.70 T and temperatures up to  $T \approx 7$  K.

Such a complex magnetic phase diagram is reminiscent of skyrmion host materials, where multiple non-collinear magnetic phases are typically found, a result of competing energy scales with comparable magnitudes [31]. For example, in most of the non-centrosymmetric B20 skyrmion compounds, the Heisenberg interaction, which favors parallel spin alignment, competes with the DM interaction, which favors orthogonal spin alignment, resulting in a non-collinear helical magnetic structure in zero magnetic field. Then the skyrmion spin structure can be realized with the application of a magnetic field. A zero field non-collinear magnetic structure seems a necessary, albeit not sufficient prerequisite for stabilizing a skyrmion state in

applied field. The square-net compound  $\text{GdRu}_2\text{Si}_2$  does show a zero field non-collinear incommensurate helical structure, and in this case a magnetic field has been shown to transform it into a skyrmion lattice [22].

To provide insight into the nature of the complex magnetism in  $\text{EuGa}_2\text{Al}_2$ , we turn to elastic neutron scattering experiments. The zero field neutron data in the  $(h, 0, l)$  scattering plane shown in Fig. 2a indicate that, upon initially cooling into the ordered phase, an incommensurate helical state forms (AFM1) with  $\mathbf{q}_{\text{inc}}$  along  $a$  and the Eu moments rotating in the  $bc$  plane as shown in Fig. 2b. At the lowest temperatures (AFM3), on the other hand, the ordering is again incommensurate with a somewhat different value of the wavevector along  $a$  (see Fig. S4), but forms a cycloid with the moments in the  $ac$  plane as shown in Fig. 2c. In the intermediate AFM2 phase, the contour map shows an increase and apparent broadening in magnetic scattering intensity. A high resolution scan in the AFM2 regime can be fit with two resolution-limited peaks (inset Fig. 2a), indicating the presence of two wavevectors associated with a mixed state between the helical and cycloidal phases. The phase assignments at high and low temperature are clearly indicated by the change in diffraction intensities between the AFM3 and AFM1 phases as shown in the scans in Fig. 2d. Recalling that neutrons only scatter from the component of the magnetization perpendicular to  $\mathbf{Q}$ , Fig. 2d compares the magnetic satellites at  $(2 \pm q_{\text{inc}}, 0, 0)$  in the AFM1 and AFM3 phases. The intensities of both incommensurate peaks approximately double when the temperature is increased from 5 K to 17 K, indicating that there is magnetic scattering from an additional spin component perpendicular to  $a$  in the AFM1 phase. In Fig. 2e, the intensities at  $(\pm q_{\text{inc}}, 0, 8)$  remain essentially unchanged between the AFM1 and AFM3 phases when  $\mathbf{Q}$  is essentially along the  $c$  axis, which indicates no significant change in the single magnetic components scattering perpendicular to  $c$ . These characteristic changes in scattering intensities demonstrate that one component of the ordered moment rotates to the  $a$ -axis on cooling, consistent with a helical phase with moments in the  $bc$  plane at 17 K transforming to a cycloid at 5 K with moments in the  $ac$  plane, in both cases with the propagation vector along  $a$ .

With AFM1 and AFM3 phases determined to be non-collinear magnetic structures but with different moment orientation, the intermediate A phase is very likely a non-coplanar magnetic phase, with skyrmion lattice being a possibility. Non-coplanar spin textures have non-zero scalar spin chirality defined as  $\chi = \mathbf{S}_i \cdot (\mathbf{S}_j \times \mathbf{S}_k)$  where  $\mathbf{S}_i, \mathbf{S}_j, \mathbf{S}_k$  are nearest neighbor spins [32]. When itinerant electrons are coupled to such a non-coplanar spin texture, they acquire a Berry phase which is proportional to  $\chi$ . Therefore, the non-coplanar spin textures produce an effective magnetic field, and additional contributions to the Hall resistivity are expected [31].

We therefore turn to field-dependent electrical trans-

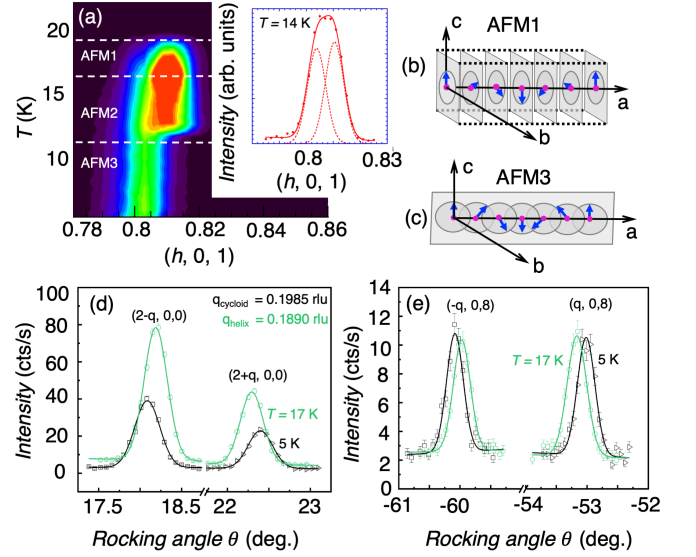


FIG. 2: Magnetic neutron diffraction results for  $\text{EuGa}_2\text{Al}_2$  in the  $(h, 0, l)$  scattering plane. (a) Contour map of the diffraction intensity around the incommensurate magnetic Bragg reflection,  $\mathbf{Q} = (\sim 0.8, 0, 1)$ , gives modulation wavevector  $\pm \mathbf{q}_{\text{inc}}$  ( $\sim 0.2, 0, 0$ ). (Inset) High resolution scan in the AFM2 regime shows substantial broadening due to scattering from two resolution-limited wave vectors in a mixed phase regime. Illustration of (b) helical and (c) cycloid magnetic phases of AFM1 and AFM3, respectively. (d) Satellites around the  $(2, 0, 0)$  fundamental Bragg peak approximately double in intensity from the AFM3 phase at 5 K to the AFM1 phase at 17 K, while (e) intensities of satellites at  $\mathbf{Q} = (\pm q_{\text{inc}}, 0, 8)$  remain essentially unchanged between AFM1 and AFM3 phases.

port measurements to shed light on the nature of the A phase in  $\text{EuGa}_2\text{Al}_2$ . In Fig. 3a we plot a subset of the measured Hall resistivity  $\rho_{yx}(H)$  ( $j \parallel a, H \parallel c$ ) for  $T = 2, 10$ , and  $20.5$  K. The full  $\rho_{yx}(H, T)$  measured manifold can be found in Fig. S2 in the Supplementary Materials. Non-linear  $\rho_{yx}(H)$  is recorded in the ordered state ( $T = 2$  K and  $10$  K), with the Hall resistivity becoming virtually linear at  $T = 20.5$  K (in the paramagnetic state).

In the presence of a non-coplanar spin texture, the Hall resistivity can be expressed as the sum of several contributions:

$$\rho_{yx} = R_0 \mu_0 H + \rho_{yx}^A + \rho_{yx}^T, \quad (1)$$

where  $R_0$  is the normal Hall coefficient,  $\rho_{yx}^A$  the anomalous Hall resistivity, and  $\rho_{yx}^T$  the topological Hall effect (THE) resistivity.  $\rho_{yx}^A$  can be estimated from an empirical scaling  $\rho_{yx}^A = S_H \rho_{xx}^2 M$  [33–35] (Fit 1, solid line in Fig. S3) which assumes a dominant intrinsic contribution due to Berry phase or extrinsic contribution due to side-jump scattering

to the anomalous Hall effect [36–38]. If, instead, the dominant extrinsic contribution is assumed to be due to skew scattering,  $\rho_{yx}^A$  has a linear dependence on  $\rho_{xx}$  (Fit 2, dashed line in Fig. S3). The two fits are qualitatively very similar, with the former being slightly better at minimizing  $\rho_{yx}^T$ .

The THE contribution,  $\rho_{yx}^T$ , is captured by the difference between the experimental data (symbols) and the fits (lines), and is plotted in Fig. 3b (see Fig. S3 for details). It appears that the THE is maximum around 1.2 T, or in the A phase, as indicated by the contour plot in the  $H - T$  phase diagram (Fig. 1d). This further supports the scenario of a non-coplanar spin texture in the A phase.

We now look into the origin of non-collinear spin textures in centrosymmetric magnetic compounds in general, and in the square-net compound  $\text{EuGa}_2\text{Al}_2$  in particular. In intermetallic compounds like  $\text{EuGa}_2\text{Al}_2$ , the Runderman-Kittel-Kasuya-Yosida (RKKY) interaction [39–41] underlines the interplay of conduction electrons and local moments. This spin-charge interaction has been shown theoretically to induce a CDW from a spin-density state [42], and was confirmed experimentally with the observation of the in-plane charge-modulation in the skyrmion state of  $\text{GdRu}_2\text{Si}_2$  [23]. However, this behavior is different in the case of  $\text{EuGa}_2\text{Al}_2$ , where the OOP CDW is perpendicular to the in-plane magnetic wavevector.

Figure 4 shows the temperature-dependent XRD measurements, which confirm that the  $\sim 50$  K anomaly previously observed in the resistivity in  $\text{EuGa}_2\text{Al}_2$  [30] is due to a CDW transition. The line-profile cuts of the XRD data around the (1, 1, 2) structural Bragg peak (Fig. 4) reveal no superlattice reflections for  $T \geq 50$  K. At  $T < 50$  K clear superlattice reflections are observed in agreement with the CDW transition temperature  $T_{CDW} \approx 50$  K established from the  $\rho(T)$  data [30]. The expected second-order CDW peaks are clearly observed in the reciprocal space maps presented in Fig. S6, S7. The temperature dependence of the superlattice reflections located at (1, 1, 2 + (-)  $q_{CDW}$ ) (Fig. 4 inset, left axis, open (closed) squares) demonstrates that the amplitude of the reflections continuously grow before sharply decreasing below  $T_N$ , then again increasing on further cooling, indicating strong spin-charge coupling. The spin-charge coupling is corroborated by the temperature dependence of  $q_{CDW}$  (Fig. 4 inset, right axis, diamonds), which increases from 0.09 reciprocal lattice units (r.l.u.) at 45 K to 0.12 r.l.u. at 25 K on cooling, before a sharp decrease is observed near  $T_N$ .  $q_{CDW}$  again increases on further cooling. Our data thus demonstrate the presence of a preformed ( $T_{CDW} > T_N$ ) OOP CDW state in  $\text{EuGa}_2\text{Al}_2$ , which persists through the magnetically ordered state, in contrast to the in-plane magnetic wavevector.

To understand the implications of the OOP CDW state on the magnetic order, we consider  $\text{EuGa}_2\text{Al}_2$  in the context of the whole  $\text{Eu}(\text{Ga}_{1-x}\text{Al}_x)_4$  series, and particu-

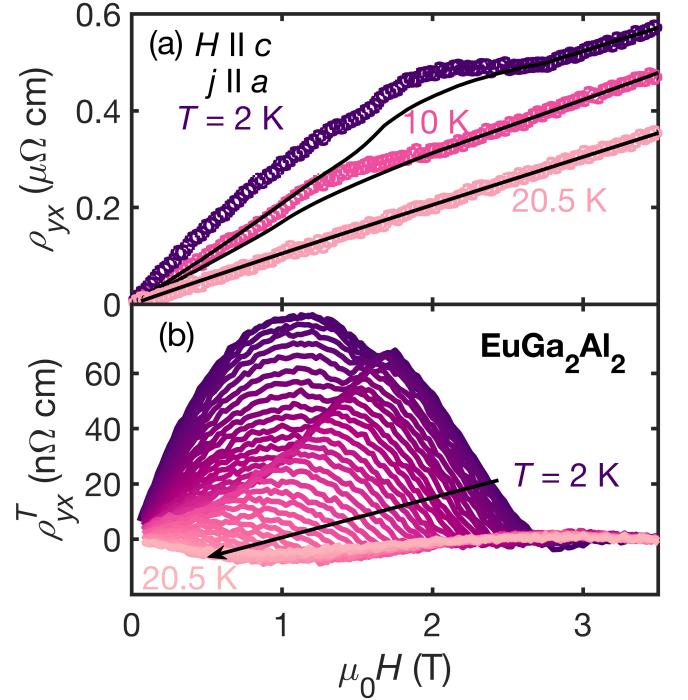


FIG. 3: Topological Hall effect in  $\text{EuGa}_2\text{Al}_2$ . (a) A subset of the measured Hall resistivity  $\rho_{yx}$  with magnetic field  $H \parallel c$  and current  $j \parallel a$  measured at  $T = 2$  K (purple circles), 10 K (magenta circles), and 20.5 K (pink circles). Solid lines are fits to Eq. S1. (b) The extracted topological Hall resistivity  $\rho_{yx}^T$  determined by subtracting the anomalous Hall resistivity  $\rho_{yx}^A$  from  $\rho_{yx}$  (see text for details) from  $T = 2$  K (purple curve) to 20.5 K (pink curve) in 0.5 K increments. The black arrow points from low to high temperature.

larly by comparison with the two end members  $\text{EuAl}_4$  and  $\text{EuGa}_4$ . The three structurally-ordered compounds  $\text{EuAl}_4$ ,  $\text{EuGa}_2\text{Al}_2$  and  $\text{EuGa}_4$  feature Eu square-net planes separated by (Ga,Al)<sub>4</sub> spacer layers. Previously, an OOP CDW transition in  $\text{EuAl}_4$  had been reported by XRD and neutron measurements near  $T_{CDW} \approx 140$  K [43, 44]. Furthermore, complex magnetism with successive magnetic transitions characterized by incommensurate ordering wave vectors had also been reported [44]. The temperature dependence of  $q_{CDW}$  shows sharp inflections at  $T_N$ , indicative of strong spin-charge coupling in  $\text{EuAl}_4$ . Importantly, the OOP CDW still persists in the  $H = 0$  magnetically order phases [43]. Although the exact magnetic structure for  $\text{EuAl}_4$  has yet to be determined, non-zero THE has recently been reported for  $H \parallel c$  [45]. By contrast,  $\text{EuGa}_4$  is distinct from both  $\text{EuGa}_2\text{Al}_2$  and  $\text{EuAl}_4$ , as it has only one magnetic transition into a simple collinear AFM structure characterized by a single commensurate propagation vector [46]. No CDW or THE is observed in  $\text{EuGa}_4$  at ambient pressure [30, 47, 48], as shown by the temperature-dependent XRD measure-



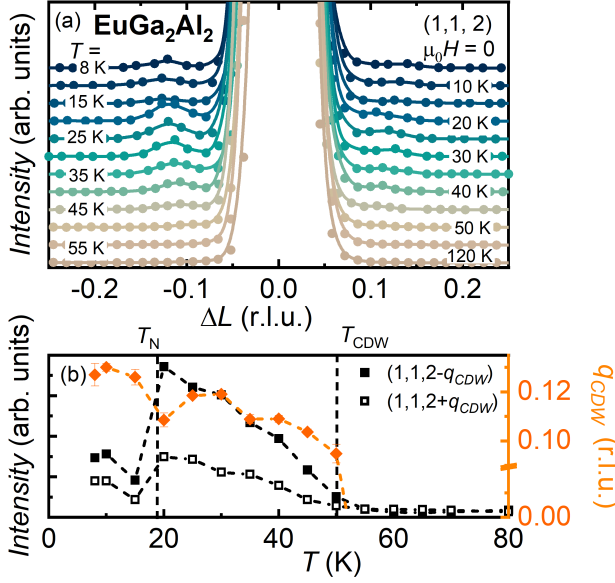


FIG. 4: XRD measurements in  $\text{EuGa}_2\text{Al}_2$ . (a) Temperature dependent line-profile cuts along  $(1, 1, 2 \pm \Delta L)$  for  $8 \leq T \leq 120$  K, with (b) showing the temperature dependence of the order parameter defined as the integrated intensity of the peak with the background subtracted, located at  $(1, 1, 2 +(-) q_{CDW})$  (left axis, open (closed) squares) and the temperature dependence of  $q_{CDW}$  (right axis, diamonds). The vertical dashed lines at  $T_N$  and  $T_{CDW}$  are determined from thermodynamic and transport measurements.

ments (Fig. S8) and transport data [48]. Together, these results suggest that the preformed incommensurate OOP CDW, which persists through the magnetically ordered state in  $\text{EuGa}_2\text{Al}_2$  and  $\text{EuAl}_4$ , is necessary for the formation of low temperature non-collinear magnetic textures. This is reinforced by the fact that, in the absence of a CDW in  $\text{EuGa}_4$ , the resulting magnetic state is a simple commensurate magnetic ordered state.

The mechanism of OOP CDWs contributing to the formation of complex in-plane magnetism can be rationalized as follows. The incommensurate magnetic phases such as those observed in  $\text{EuGa}_2\text{Al}_2$  are low-energy ordered states, and their instability can be related to the nesting properties of the Fermi surface in metals. The peak location of the bare magnetic susceptibility dictates the wave vector and thus the noncollinear spin texture. In  $\text{EuGa}_2\text{Al}_2$  (and  $\text{EuAl}_4$ ), the preformed CDW above  $T_N$  necessarily leads to a Fermi surface reconstruction and consequently modifies the landscape of the bare susceptibility. The OOP CDW results in band foldings in the OOP direction which effectively reduces the dimensionality of the Fermi surface (*i.e.* renders it more two-dimensional), leaving the system more susceptible to the formation of a noncollinear spin texture with in-plane propagation vector. This is in contrast to  $\text{EuGa}_4$  with no CDW where the Fermi surface

is necessarily more three-dimensional. Our results thus indicate that the OOP CDW in the square-net compounds favor the formation of non-collinear spin textures, which in turn set the stage for non-coplanar spin textures with the application of a magnetic field.

In conclusion, we determine the  $\text{EuGa}_2\text{Al}_2$  magnetic phase diagram for  $H \parallel c$  by magnetization and resistivity measurements. Three zero field magnetic phases are present in the antiferromagnetic ordered state. With the application of a magnetic field  $H \parallel c$ , a new magnetic phase A emerges, separating the AFM3 and AFM1 phases. Neutron diffraction measurements in zero field reveal a cycloid spin structure in AFM3 with an incommensurate propagation vector in the  $a$  direction, while an incommensurate helical structure propagating in the same direction is observed in AFM1. The transition between these two noncollinear magnetic spin states takes place *via* the A phase in applied magnetic field, and gives rise to the observed THE which is maximized in this intermediate phase. Our XRD measurements reveal a preformed incommensurate OOP CDW propagating along the  $c$  direction emerging below 50 K which persists into the magnetically ordered state. Taken in context with the isostructural compounds  $\text{EuAl}_4$  and  $\text{EuGa}_4$ , our results point to the OOP CDW as a possible driving mechanism in stabilizing non-collinear spin textures, which in turn can give way to non-coplanar or even skyrmion spin textures with the application of magnetic field.

## ACKNOWLEDGEMENTS

JMM was supported by the National Science Foundation (NSF) Graduate Research Fellowship under Grant DGE 1842494. EM and SL acknowledge support from U.S. DOE BES DE- SC0019503. KJA was supported by NSF DMR 1903741. XRD measurements were supported by the U.S. Department of Energy, Office of Basic Energy Sciences Grant No. DE-FG02-06ER46285. P. A. acknowledges the Gordon and Betty Moore Foundation's EPiQS Initiative through Grants No. GBMF9452. This research used resources at the High Flux Isotope Reactor, Oak Ridge National Laboratory, and the Advanced Photon Source, Argonne National Laboratory, which are DOE Office of Science User Facilities supported by the US Department of Energy, Office of Science, Office of Basic Energy Sciences. Work at the Materials Science Division, Argonne National Laboratory (single crystal diffuse x-ray scattering) was supported by US Department of Energy, Office of Science, Office of Basic Energy Sciences, Materials Sciences and Engineering Division. The use of the EPMA facility at the Department of Earth Science, Rice University, Houston, Texas, is kindly acknowledged. The identification of any commercial product or trade name does not imply endorsement or recommendation by the National Institute of Standards and Technology.

\* sl160@rice.edu

† em11@rice.edu

- [1] N. Nagaosa and Y. Tokura, *Nature nanotechnology* **8**, 899 (2013).
- [2] A. Fert, V. Cros, and J. Sampaio, *Nature nanotechnology* **8**, 152 (2013).
- [3] A. Fert, N. Reyren, and V. Cros, *Nature Reviews Materials* **2**, 1 (2017).
- [4] K. M. Song, J.-S. Jeong, B. Pan, X. Zhang, J. Xia, S. Cha, T.-E. Park, K. Kim, S. Finizio, J. Raabe, *et al.*, *Nature Electronics* **3**, 148 (2020).
- [5] F. Jonietz, S. Mühlbauer, C. Pfleiderer, A. Neubauer, W. Münzer, A. Bauer, T. Adams, R. Georgii, P. Böni, R. A. Duine, *et al.*, *Science* **330**, 1648 (2010).
- [6] S. Mühlbauer, B. Binz, F. Jonietz, C. Pfleiderer, A. Rosch, A. Neubauer, R. Georgii, and P. Böni, *Science* **323**, 915 (2009).
- [7] X. Yu, N. Kanazawa, Y. Onose, K. Kimoto, W. Zhang, S. Ishiwata, Y. Matsui, and Y. Tokura, *Nature materials* **10**, 106 (2011).
- [8] S. Seki, X. Yu, S. Ishiwata, and Y. Tokura, *Science* **336**, 198 (2012).
- [9] T. Adams, A. Chacon, M. Wagner, A. Bauer, G. Brandl, B. Pedersen, H. Berger, P. Lemmens, and C. Pfleiderer, *Physical review letters* **108**, 237204 (2012).
- [10] I. Dzyaloshinsky, *Journal of Physics and Chemistry of Solids* **4**, 241 (1958).
- [11] T. Moriya, *Physical Review Letters* **4**, 228 (1960).
- [12] T. Okubo, S. Chung, and H. Kawamura, *Phys. Rev. Lett.* **108**, 017206 (2012).
- [13] A. O. Leonov and M. Mostovoy, *Nature Communications* **6**, 8275 (2015).
- [14] S.-Z. Lin and S. Hayami, *Physical Review B* **93**, 064430 (2016).
- [15] S. Heinze, K. Von Bergmann, M. Menzel, J. Brede, A. Kubetzka, R. Wiesendanger, G. Bihlmayer, and S. Blügel, *Nature Physics* **7**, 713 (2011).
- [16] C. D. Batista, S.-Z. Lin, S. Hayami, and Y. Kamiya, *Reports on Progress in Physics* **79**, 084504 (2016).
- [17] R. Ozawa, S. Hayami, and Y. Motome, *Physical Review Letters* **118**, 147205 (2017).
- [18] S. Hayami, R. Ozawa, and Y. Motome, *Physical Review B* **95**, 224424 (2017).
- [19] T. Kurumaji, T. Nakajima, M. Hirschberger, A. Kikkawa, Y. Yamasaki, H. Sagayama, H. Nakao, Y. Taguchi, T.-h. Arima, and Y. Tokura, *Science* **365**, 914 (2019).
- [20] M. Hirschberger, L. Spitz, T. Nomoto, T. Kurumaji, S. Gao, J. Masell, T. Nakajima, A. Kikkawa, Y. Yamasaki, H. Sagayama, *et al.*, *Physical Review Letters* **125**, 076602 (2020).
- [21] M. Hirschberger, T. Nakajima, S. Gao, L. Peng, A. Kikkawa, T. Kurumaji, M. Kriener, Y. Yamasaki, H. Sagayama, H. Nakao, *et al.*, *Nature communications* **10**, 1 (2019).
- [22] N. D. Khanh, T. Nakajima, X. Yu, S. Gao, K. Shibata, M. Hirschberger, Y. Yamasaki, H. Sagayama, H. Nakao, L. Peng, *et al.*, *Nature Nanotechnology* , 1 (2020).
- [23] Y. Yasui, C. J. Butler, N. D. Khanh, S. Hayami, T. Nomoto, T. Hanaguri, Y. Motome, R. Arita, T.-h. Arima, Y. Tokura, *et al.*, *Nature communications* **11**, 1 (2020).
- [24] S. Ishiwata, M. Tokunaga, Y. Kaneko, D. Okuyama, Y. Tokunaga, S. Wakimoto, K. Kakurai, T. Arima, Y. Taguchi, and Y. Tokura, *Physical Review B* **84**, 054427 (2011).
- [25] S. Ishiwata, T. Nakajima, J.-H. Kim, D. Inosov, N. Kanazawa, J. White, J. Gavilano, R. Georgii, K. Seemann, G. Brandl, *et al.*, *Physical Review B* **101**, 134406 (2020).
- [26] T. Nomoto, T. Koretsune, and R. Arita, *Phys. Rev. Lett.* **125**, 117204 (2020).
- [27] S. Hayami and Y. Motome, *arXiv preprint arXiv:2010.14671* (2020).
- [28] Z. Wang, Y. Su, S.-Z. Lin, and C. D. Batista, *Physical Review B* **103**, 104408 (2021).
- [29] M. Ślaski, A. Szytuła, J. Leciejewicz, and A. Zygmunt, *Journal of magnetism and magnetic materials* **46**, 114 (1984).
- [30] M. Stavinoha, J. A. Cooley, S. G. Minasian, T. M. McQueen, S. M. Kauzlarich, C.-L. Huang, and E. Morosan, *Physical Review B* **97**, 195146 (2018).
- [31] Y. Tokura and N. Kanazawa, *Chemical Reviews* (2020).
- [32] K. Ueda, S. Iguchi, T. Suzuki, S. Ishiwata, Y. Taguchi, and Y. Tokura, *Physical review letters* **108**, 156601 (2012).
- [33] N. Kanazawa, Y. Onose, T. Arima, D. Okuyama, K. Ohoyama, S. Wakimoto, K. Kakurai, S. Ishiwata, and Y. Tokura, *Physical review letters* **106**, 156603 (2011).
- [34] P. Puphal, V. Pomjakushin, N. Kanazawa, V. Ukleev, D. J. Gawryluk, J. Ma, M. Naamneh, N. C. Plumb, L. Keller, R. Cubitt, *et al.*, *Physical Review Letters* **124**, 017202 (2020).
- [35] Y. Xu, L. Das, J. Ma, C. Yi, S. Nie, Y. Shi, A. Tiwari, S. Tsirkin, T. Neupert, M. Medarde, *et al.*, *Physical Review Letters* **126**, 076602 (2021).
- [36] N. Nagaosa, J. Sinova, S. Onoda, A. H. MacDonald, and N. P. Ong, *Reviews of modern physics* **82**, 1539 (2010).
- [37] M. Lee, Y. Onose, Y. Tokura, and N. Ong, *Physical Review B* **75**, 172403 (2007).
- [38] Y. Li, N. Kanazawa, X. Yu, A. Tsukazaki, M. Kawasaki, M. Ichikawa, X. Jin, F. Kagawa, and Y. Tokura, *Physical Review Letters* **110**, 117202 (2013).
- [39] M. A. Ruderman and C. Kittel, *Physical Review* **96**, 99 (1954).
- [40] T. Kasuya, *Progress of theoretical physics* **16**, 45 (1956).
- [41] K. Yosida, *Physical Review* **106**, 893 (1957).
- [42] S. Hayami and Y. Motome, *arXiv preprint arXiv:2108.04997* (2021).
- [43] S. Shimomura, H. Murao, S. Tsutsui, H. Nakao, A. Nakamura, M. Hedo, T. Nakama, and Y. Onuki, *Journal of the Physical Society of Japan* **88**, 014602 (2019).
- [44] K. Kaneko, T. Kawasaki, A. Nakamura, K. Munakata, A. Nakao, T. Hanashima, R. Kiyonagi, T. Ohhara, M. Hedo, T. Nakama, *et al.*, *Journal of the Physical Society of Japan* **90**, 064704 (2021).
- [45] T. Shang, Y. Xu, D. Gawryluk, J. Ma, T. Shiroka, M. Shi, and E. Pomjakushina, *Physical Review B* **103**, L020405 (2021).
- [46] T. Kawasaki, K. Kaneko, A. Nakamura, N. Aso, M. Hedo, T. Nakama, T. Ohhara, R. Kiyonagi, K. Oikawa,

- I. Tamura, *et al.*, Journal of the Physical Society of Japan **85**, 114711 (2016).
- [47] A. Nakamura, T. Uejo, F. Honda, T. Takeuchi, H. Harima, E. Yamamoto, Y. Haga, K. Matsubayashi, Y. Uwatoko, M. Hedo, *et al.*, Journal of the Physical Society of Japan **84**, 124711 (2015).
- [48] K. Allen and et al, In Preperation (2021).
- [49] J. Rodríguez-Carvajal, Physica B: Condensed Matter **192**, 55 (1993).
- [50] M. J. Krogstad, S. Rosenkranz, J. M. Wozniak, G. Jennings, J. P. Ruff, J. T. Vaughey, and R. Osborn, Nature materials **19**, 63 (2020).

# Supplemental Materials: Incommensurate magnetic orders and possible field-induced skyrmion state in the square-net centrosymmetric $\text{EuGa}_2\text{Al}_2$ system

## HALL RESISTIVITY ANALYSIS

AC electrical transport measurements were performed in Quantum Design (QD) DynaCool equipped with the Electrical Transport Option (ETO) and magnetization measurements were taken in a QD Dynacool with vibrating sample magnetometer option (VSM). The tetragonal crystal symmetry dictates that the crystallographic  $a$  and  $b$  are equivalent. Throughout the manuscript, current  $j \parallel a$  is applied while  $H \parallel c$ . All contact resistances were measured to be less than  $2 \Omega$  at room temperature. Typical measurement parameters used were current  $j = 5 \text{ mA}$  and frequency  $f = 9.15 \text{ Hz}$ . The as-measured field-dependent resistivity was symmetrized and the corresponding Hall resistivity  $\rho_{yx}$  was antisymmetrized.

Magnetization as a function of magnetic field  $M(H)$  was measured by sweeping the field from  $0 \rightarrow 3.5 \text{ T}$  (closed symbols, Fig. S1a) then back  $3.5 \rightarrow 0 \text{ T}$  (open symbols in Fig. S1). No observable hysteresis is seen in  $M(H)$  in any region of the phase diagram (Fig. 1e) for which we have plotted three representative temperatures  $T = 2 \text{ K}$  (purple symbols),  $T = 15 \text{ K}$  (magenta symbols), and  $T = 17 \text{ K}$  (pink symbols), suggesting no strongly first order phase transitions. The field dependent transverse and Hall resistivity,  $\rho_{xx}$  and  $\rho_{yx}$ , are shown in Fig. S1b and c, respectively. No observable hysteresis is seen. For consistency, all data plotted in the manuscript and the corresponding analysis are done with data corresponding to field sweeps from  $0 \rightarrow 3.5 \text{ T}$ , except in Fig. S1.,

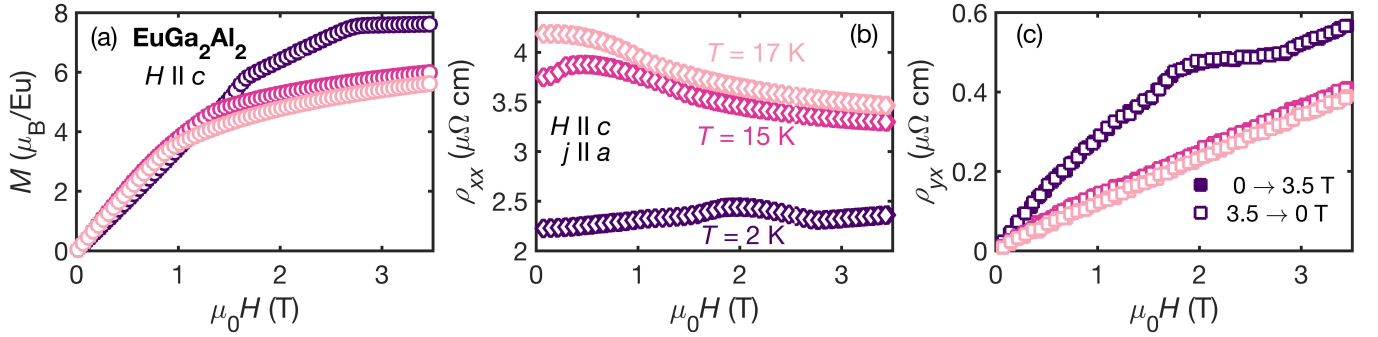


FIG. S1: (a) Magnetic field dependent magnetization measured for increasing field (closed symbols) and decreasing field (open symbols) at temperatures  $T = 2 \text{ K}$  (purple),  $15 \text{ K}$  (magenta symbols), and  $17 \text{ K}$  (pink symbols). Magnetic field dependent (b) transverse resistivity  $\rho_{xx}$  and (c) Hall resistivity  $\rho_{yx}$  for  $\mu_0 H$   $0 \rightarrow 3.5 \text{ T}$  (closed symbols) and  $\mu_0 H$   $3.5 \rightarrow 0 \text{ T}$  (open symbols) measured at  $T = 2 \text{ K}$  (purple symbols),  $15 \text{ K}$  (magenta symbols), and  $17 \text{ K}$  (pink symbols).

Figure S2 outlines the method for determining  $\rho_{yx}^T$  for  $H \parallel c$  and  $j \parallel a$ .  $M(H)$  (Fig. S2a),  $\rho_{xx}$  (Fig. S2b) and  $\rho_{yx}$  (Fig. S2c) were measured from  $T = 2 \text{ K}$  to  $20.5 \text{ K}$  in  $0.5 \text{ K}$  increments for  $0 < \mu_0 H < 3.5 \text{ T}$ . Spin reorientation transitions are marked by local maxima in  $dM/dH$  and  $d\rho_{xx}/dH$ , as exemplified by the data at  $T = 2 \text{ K}$  (Fig. S2d,e).  $\rho_{yx}^T$  in Fig. S2f is determined after subtracting the normal Hall contribution  $R_0\mu_0 H$  and the anomalous contribution  $S_H\rho_{xx}^2 M$  from the measured  $\rho_{yx}$  in Fig. S2c as described next.

The anomalous contribution to the Hall resistivity,  $\rho_{yx}^A$ , can either be expressed as  $S_H\rho_{xx}^2 M$  for a dominant intrinsic scattering mechanism or  $S'_H\rho_{xx}M$  for skew scattering. The intrinsic mechanism is expected to dominate in moderately disordered systems, while the skew scattering mechanism is expected to dominate in ultraclean systems [36]. We compared the fits to the measured  $\rho_{yx}$  data using both empirical expressions. For Fit 1 we assume a dominant intrinsic mechanism, and fit the data in the spin polarized state where  $M$  saturates, therefore  $\rho_{yx}^T$  becomes negligible, and  $\rho_{yx}$  is linear to

$$\frac{\rho_{yx}}{\mu_0 H} = R_0 + \frac{S_H \rho_{xx}^2 M}{\mu_0 H}. \quad (\text{S1})$$

Here,  $R_0$  is extracted as the intercept and  $S_H$  is the slope of the linear fit when plotting  $\rho_{yx}/\mu_0 H$  vs.  $S_H\rho_{xx}^2 M/\mu_0 H$ . Similarly, for Fit 2, assuming skew scattering is the dominant mechanism, the same data in the field polarized regime are fit to



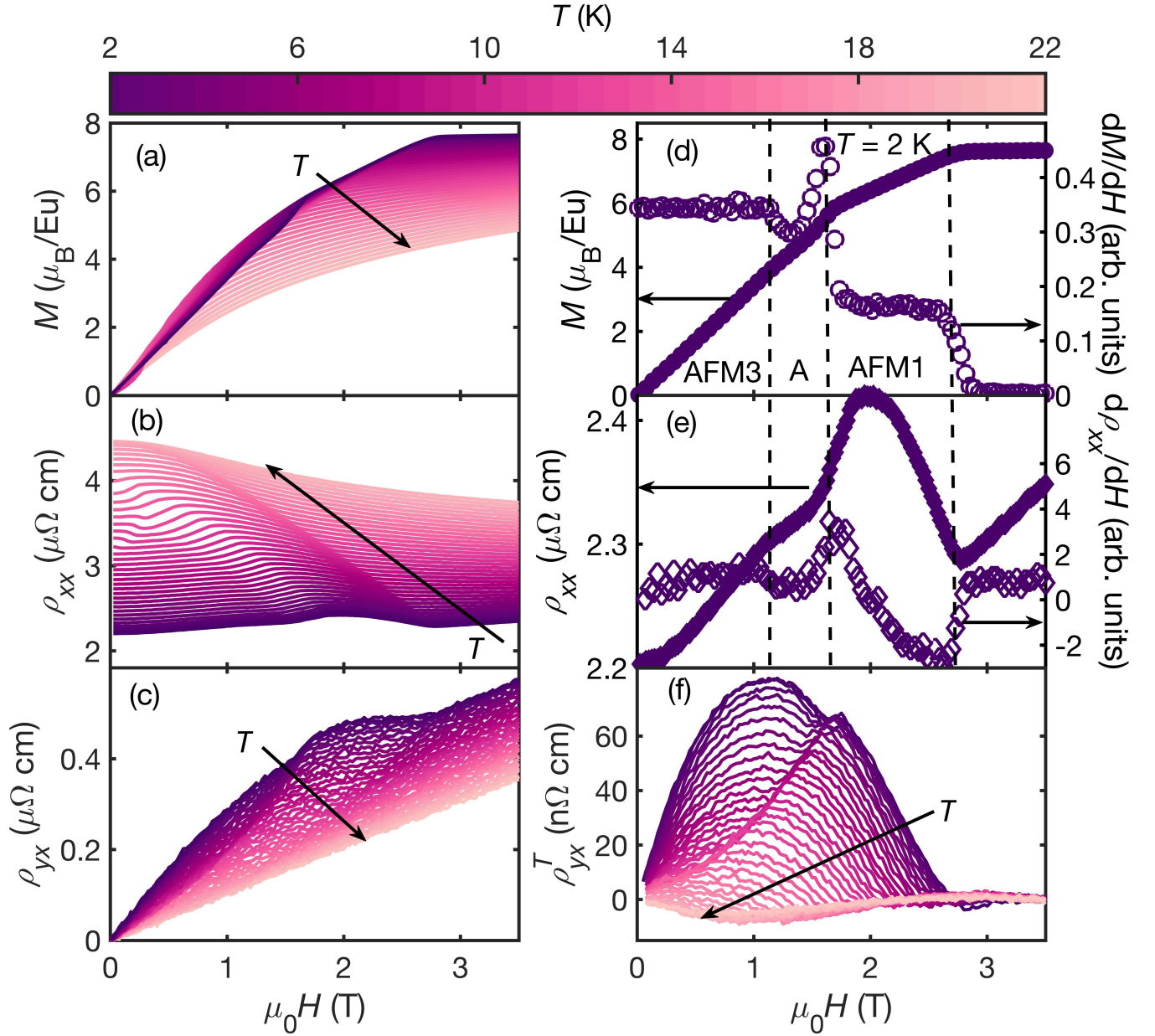


FIG. S2: Determination of the topological Hall resistivity. Field dependent (a) magnetization  $M$ , (b) resistivity  $\rho_{xx}$ , and (c) Hall resistivity  $\rho_{yx}$  measured from  $T = 2$  K (purple lines) to 20.5 K (pink line) in 0.5 K increments. All data are measured with magnetic field  $H \parallel c$  and transport data are measured with current  $j \parallel a$ . (d)  $M$  measured at  $T = 2$  K (left axis, closed circles) and the corresponding differential magnetic susceptibility  $dM/dH$  (right axis, open circles). (e)  $\rho_{xx}$  measured at  $T = 2$  K (left axis, closed diamonds) and the derivative  $d\rho_{xx}/dH$  (right axis, open diamonds). (f) The extracted topological Hall resistivity  $\rho_{yx}^T$ .

$$\frac{\rho_{yx}}{\mu_0 H} = R_0 + \frac{S_H \rho_{xx} M}{\mu_0 H}. \quad (\text{S2})$$

The results of the two fits are plotted in Fig. S3a as a solid and dashed line, respectively, for  $T = 2$  K. Subtractions of the fits from the measured  $\rho_{yx}$  data give the  $\rho_{yx}^T$  values, which are plotted for all measured temperatures in Fig. S3b (Fit 1) and Fig. S3c (Fit 2). The shapes of  $\rho_{yx}^T$  extracted in two scenarios are similar, but assuming an intrinsic contribution does a slightly better job of minimizing  $\rho_{yx}^T$ .

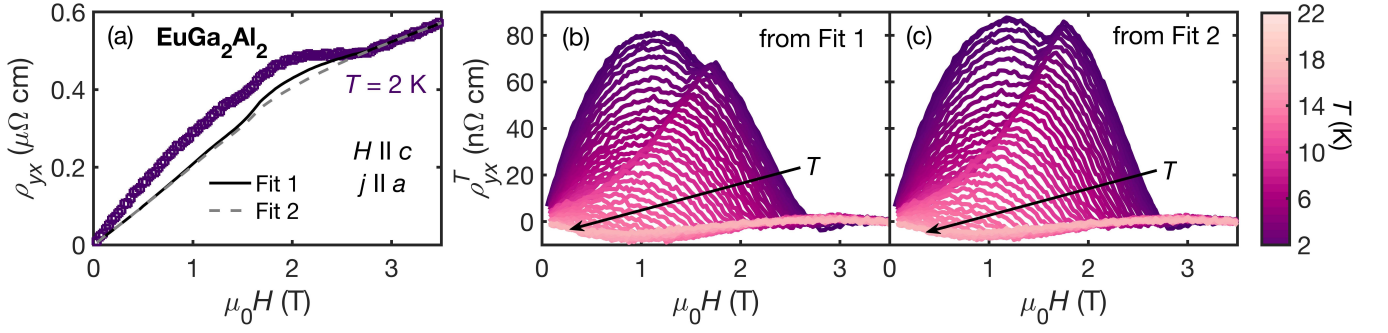


FIG. S3: (a) Hall resistivity  $\rho_{yx}$  measured with magnetic field  $H \parallel c$  and current  $j \parallel a$  at temperature  $T = 2 \text{ K}$  (open symbols) and fits to Eq. S1 (solid line) versus Eq. S2 (dashed line). Field dependence of the topological Hall resistivity  $\rho_{yx}^T$  extracted from (b) Fit 1 and (c) Fit 2 (see text for details) as a function of field from  $T = 2 \text{ K}$  to  $20.5 \text{ K}$  in  $0.5 \text{ K}$  steps.

### NEUTRON DATA

The neutron scattering experiments were carried out on the HB-3 triple axis spectrometer at the High Flux Isotope Reactor at Oak Ridge National Laboratory. The single crystal was in the shape of a flat plate of thickness  $0.53 \text{ mm}$  and weighed  $48 \text{ mg}$ . Most of the data were obtained using pyrolytic graphite (PG) filter and PG(002) monochromator at  $35 \text{ meV}$  incident and scattered neutron energies to reduce the very high absorption for Eu, and collimations of  $48^\circ\text{'-}40^\circ\text{'-}40^\circ\text{'-}120^\circ\text{'}$  full-width-at-half-maximum (FWHM). Data were collected in the  $(h, h, l)$ ,  $(h, k, 0)$ , and  $(h, 0, l)$  scattering planes. A limited set of high resolution data were collected using the Si(111) monochromator with an energy of  $9 \text{ meV}$  and collimations of  $48^\circ\text{'-}20^\circ\text{'-}20^\circ\text{'-}30^\circ\text{'}$  FWHM. A closed cycle refrigerator with a base temperature of  $4.5 \text{ K}$  was employed for the sample environment.

Data were collected in the  $(h, h, l)$ ,  $(h, k, 0)$ , scattering planes to search for other possible incommensurate magnetic peaks and to establish that the observed incommensurate wave vector is strictly along the  $[1, 0, 0]$  direction. In the  $(h, 0, l)$  scattering plane, 27 magnetic Bragg reflections were collected as a function of rocking angle ( $\theta$ ) at temperatures  $T = 5 \text{ K}$  and  $17 \text{ K}$  to be used in the magnetic structure analysis of the high temperature AFM1 and low temperature AFM3 phases. Integrated intensities were corrected for instrument resolution and the heavy absorption of Eu. Absorption corrections were calculated assuming a flat plate geometry, where the tetragonal  $a$ -axis lies in the plane of the crystal face and the  $c$ -axis is normal to the plane. Correction ratios were rejected if the total path length for incoming and outgoing beams became longer than  $0.5$  times the crystal width ( $w = 6 \text{ mm}$ ), viz.  $r_i + r_f = r_T \geq 0.5w$ . Magnetic intensities were discarded from the refinement for interference with Al and Cu powder peaks, unphysical absorption corrections, and/or inability to measure a nearby nuclear Bragg peak for normalization. Refinements were carried out using the FullProf Suite [49]. Wavevector  $\mathbf{Q}$  and incommensurate reduced wavevector  $\mathbf{q}_{inc}$  are quoted in reciprocal lattice units (r.l.u.) where  $a^* = 2\pi/a$  and  $c^* = 2\pi/c$  with  $a = 4.3119 \text{ Angstroms}$  and  $c = 10.8939 \text{ Angstroms}$ .

In the AFM2 phase the width of the peak exhibits some broadening even on employing coarse resolution. We therefore tightened the collimation to the best available at the time,  $48^\circ\text{'-}20^\circ\text{'-}20^\circ\text{'-}70^\circ\text{'}$ , and those data are shown in Fig. S4. In the AFM1 and AFM3 phase the peaks are resolution limited, while the broader peak in the AFM2 regime can be fit with two resolution-limited peaks, indicating a first-order transition between AFM1 and AFM2 phases that overlap. We also carried out an experiment using the Si(111) monochromator with  $9 \text{ meV}$  incident energy and tight collimation, but given the limited statistics in that configuration it was not possible to obtain improved data.

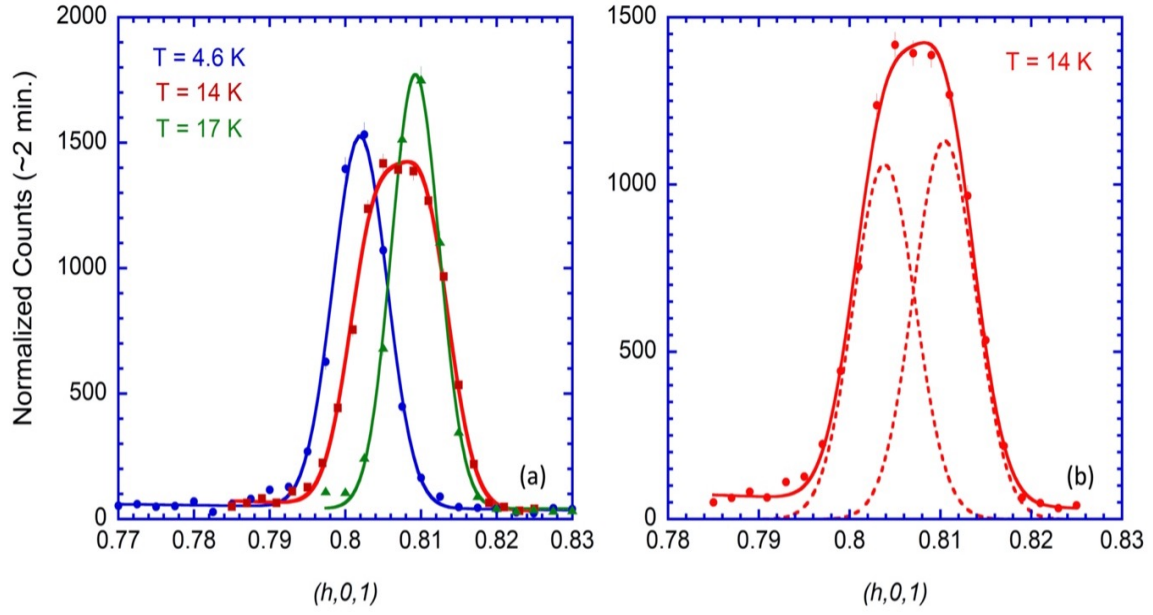


FIG. S4: (a) High resolution neutron diffraction scans along  $(h, 0, 1)$  in each of the three phase regimes AFM3, AFM2, and AFM1 at  $T = 4.6, 14, 17$  K, respectively. (b) The scan in the AFM2 regime has the largest integrated intensity because of its breadth, and can be fit with two resolution-limited Gaussian peaks, indicating that the two types of magnetic order coexist in this mixed regime with a first-order transition between the high temperature helical and low temperature cycloid phases.

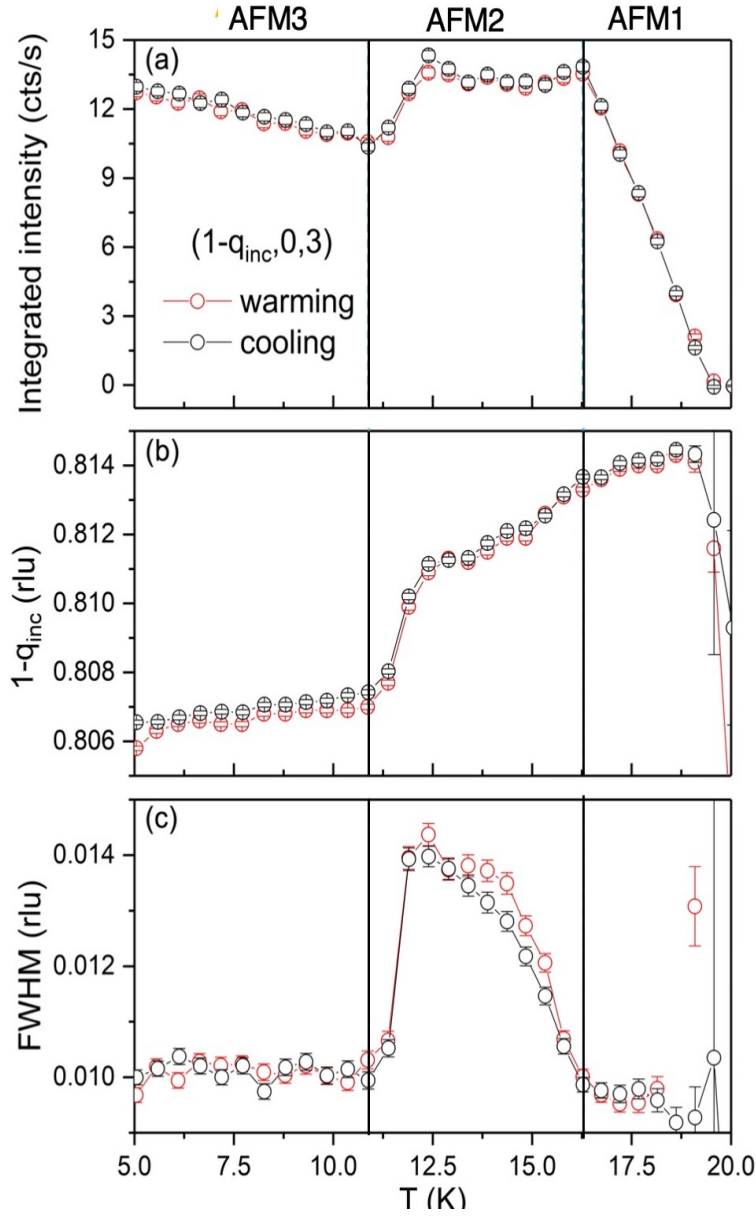


FIG. S5: Temperature dependence on warming and cooling of the incommensurate magnetic peak(s) near  $\mathbf{Q} = (0.8, 0, 3)$  extracted using a single Gaussian fit to the data at each temperature. Lines are guides to the eye. (a) The integrated intensity, proportional to the square of the order parameter, illuminates three distinct phase regimes. A simple mean-field fit gives a transition temperature of  $T_N = 19.5(2)$  K from the paramagnetic to AFM1 phase. (b) The wavevector peak position,  $1-\mathbf{q}_{inc}$ , and (c) full width at half maximum display sharp jumps on warming or cooling on entering the AFM2 regime. The sudden increase in each parameter moving from the ground state AFM3 to AFM2 can be attributed to a first-order transition where a new wavevector emerges, yielding a mixed phase state between AFM3 and AFM2. With further increase in temperature, the intensity of the AFM3 wavevector peak falls off in favor of the new AFM1 wavevector, illustrated by the narrowing of the AFM2 peak in (c).

# TEMPERATURE DEPENDENT X-RAY DIFFRACTION DATA

X-ray diffraction measurements shown in Fig. 4 of the main text were performed with a low-emittance Xenocs GeniX 3D, Mo  $K_\alpha$  (17.4 keV) source in an in-house set-up. A Huber four-circle diffractometer was used to control sample motion. A Mar345 image plate detector consisting of  $12 \times 10^6$  pixels was used as a detector. The sample was cooled by closed-cycle cryostat with Be domes functioning as both vacuum and radiation shields to a base temperature of 8 K.

A three-dimensional survey of momentum space was performed by moving the crystal through an angular range of  $20^\circ$  in  $\theta$  to index the crystal. After the CDW peak was located, a temperature-dependent series of three-dimensional surveys of momentum space were collected by moving the crystal through a smaller range of  $\theta$  at sample temperatures between 8 K and 120 K.

The data collected were centered about the (1,1,2) Bragg peak. Line cuts were taken along the  $L$  direction from 1.516 r.l.u. to 2.262 r.l.u. at each temperature.  $H$  and  $K$  values were accurate within 0.01 r.l.u. The intensities in Fig. 4b were integrated along the line cuts in Fig. 4a around each CDW peak after subtracting the background.

All other X-ray diffraction data were collected in the following way. Three-dimensional volumes of diffuse X-ray scattering were collected at the Advanced Photon Source on sector 6-ID-D using an incident energy of 87.1 keV on  $\text{EuGa}_2\text{Al}_2$ ,  $\text{EuGa}_4$ , and  $\text{EuAl}_4$ . Sample temperatures from 300 K to 30 K were controlled by a nitrogen or helium gas flow. During the measurements, the samples were continuously rotated about an axis perpendicular to the beam at  $1^\circ \text{ s}^{-1}$  over  $360^\circ$ , with images recorded every 0.1 s on a DECTRIS Pilatus 2M detector with a 1-mm-thick CdTe sensor layer. These were transformed to reciprocal space coordinates, allowing  $S(Q)$  to be determined over a range of  $\pm 15 \text{ \AA}^{-1}$  in all directions. Further details are given in Ref. [50].

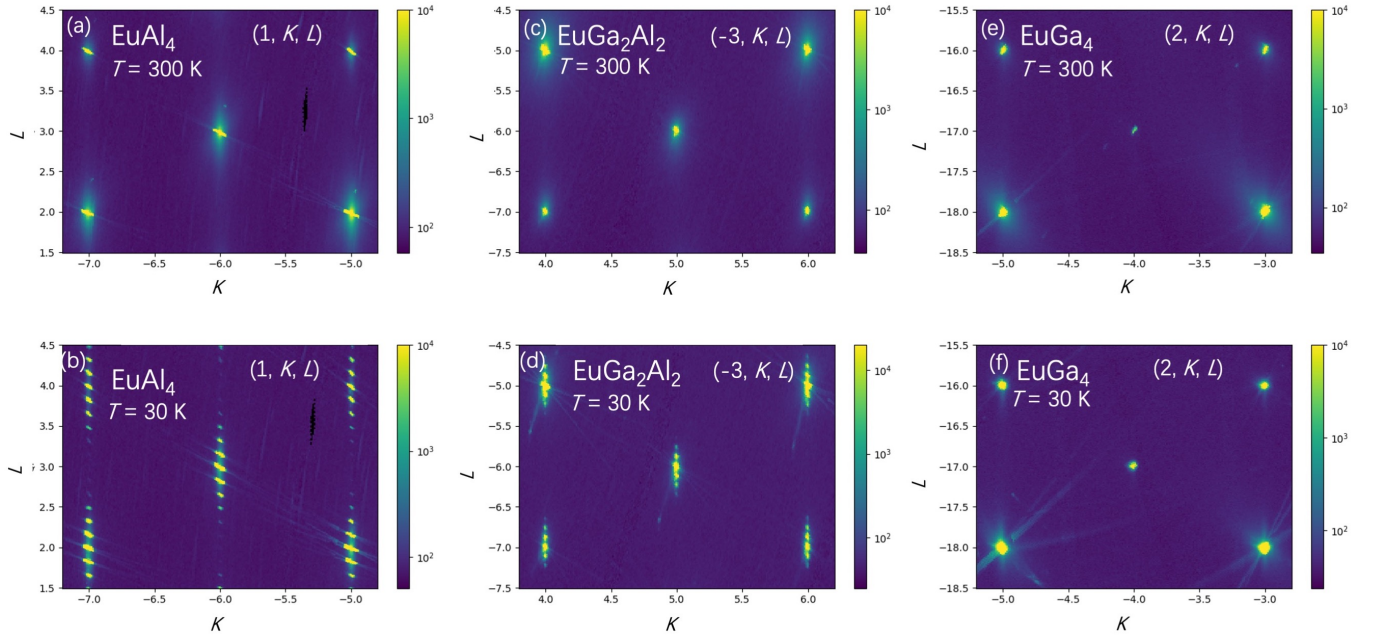


FIG. S6: X-ray diffraction reciprocal space maps. Reciprocal space maps in the  $(1, K, L)$  scattering plane of  $\text{EuAl}_4$  at (a) 300 K and (b) 30 K. Clear superlattice reflections are observed forming along the  $(0,0,L)$  direction at 30 K. Reciprocal space maps in the  $(-3, K, L)$  scattering plane of  $\text{EuGa}_2\text{Al}_2$  at (c) 300 K and (d) 30 K. Again superlattice reflections are observed forming along the  $(0,0,L)$  direction at 30 K. Reciprocal space maps in the  $(2, K, L)$  scattering plane of  $\text{EuGa}_4$  at (e) 300 K and (f) 30 K. No superlattice reflections are observed down to 30 K.



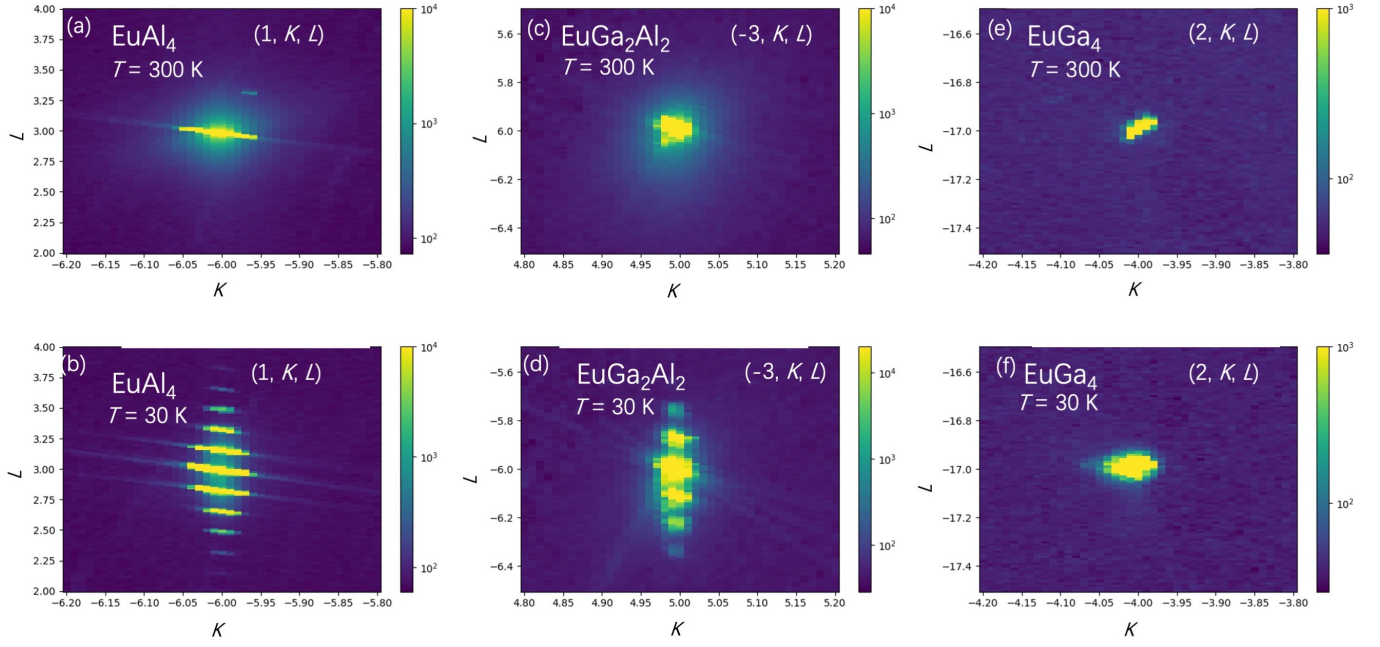


FIG. S7: High resolution X-ray diffraction reciprocal space maps corresponding to Fig. S6 for  $\text{EuAl}_4$  at 300 and 30 K (a,b),  $\text{EuGa}_2\text{Al}_2$  at 300 and 30 K (c,d), and  $\text{EuGa}_4$  at 300 and 30 K (e,f).

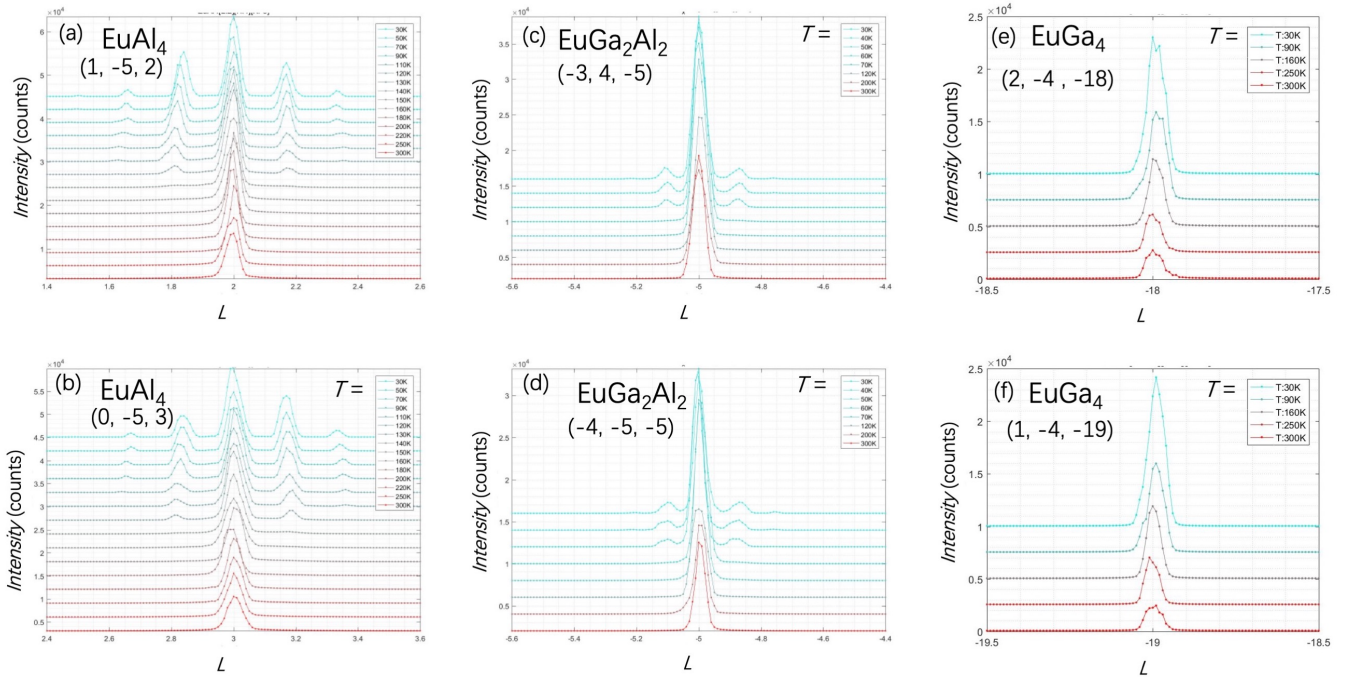


FIG. S8: Temperature-dependent line cuts of high resolution X-ray diffraction data between 300 and 30 K around the (a)  $(1, -5, 2)$  nuclear Bragg peak and (b)  $(0, -5, 3)$  nuclear Bragg peak of  $\text{EuAl}_4$ . Superlattice reflections emerge near the  $T = 140$  K providing evidence for CDW behavior consistent with previous reports [43, 44]. Line cuts near the (c)  $(-3, 4, -5)$  and (d)  $(-4, -5, -5)$  nuclear Bragg peaks of  $\text{EuGa}_2\text{Al}_2$  giving evidence for CDW behavior discussed in the main text. Line cuts near the (e)  $(2, -4, -18)$  and (f)  $(1, -4, -19)$  nuclear Bragg peak of  $\text{EuGa}_4$ . No evidence superlattice reflections are observed and hence no evidence for a CDW is observed for temperatures above 30 K.